

# Single-Image Superresolution Through Directional Representations

Wojciech Czaja, James M. Murphy, Daniel Weinberg

---

## Abstract

We develop a mathematically-motivated algorithm for image superresolution, based on the discrete shearlet transform. The shearlet transform is strongly directional, and is known to provide near-optimally sparse representations for a broad class of images. This often leads to superior performance in edge detection and image representation, when compared to other isotropic frames. We justify the use of shearlet frames for superresolution mathematically before presenting a superresolution algorithm that combines the shearlet transform with the sparse mixing estimators (SME) approach pioneered by Mallat and Yu. Our algorithm is compared with an isotropic superresolution method, a previous prototype of a shearlet superresolution algorithm, and SME superresolution with a discrete wavelet frame. Our numerical results on a variety of image types show strong performance in terms of PSNR.

---

## 1. Introduction

Superresolution is the problem of increasing the resolution of an image without introducing artifacts. It is a significant problem in image processing, and in related scientific applications, including medical imaging [1, 2, 3, 4] and remote sensing [5, 6, 7, 8]. An interdisciplinary problem, superresolution has been approached from a variety of standpoints. Mathematicians and statisticians often frame the problem in terms of recovering high frequency information from a signal that has been degraded. In this way, superresolution can be considered as an inverse problem.

In our formulation, we aim to recover an image signal  $f : [0, 1]^2 \rightarrow \mathbb{R}$  given measurements

$$y = \mathcal{L}(f) + \mathcal{N}, \tag{1}$$

where  $\mathcal{L}$  is a degradation operator and  $\mathcal{N}$  is a noise term. For example,  $\mathcal{L}$  may be understood as a downsampling or convolutional blur operator and  $\mathcal{N}$  as Gaussian noise. In this context, the goal of

superresolution is to recover the original image by increasing the resolution and denoising.

Mathematicians and statisticians often aim to prove theoretical guarantees for such an inverse problem and related discretizations on a certain model class of signals. This has led to much rich theory in recent years, particularly within the harmonic analysis community [9, 10, 11, 12, 13, 14, 15]. Many of these works prove theoretical guarantees for recovery even with only limited, low-frequency measurements. However, these results are often of a continuous nature, making the numerical implementation of the theoretical ideas difficult. Other theories are discrete, but pertain to a restrictive model class of signals that do not represent images of great interest to scientists.

In particular, the electrical and computer engineering communities have produced a plethora of superresolution algorithms that employ a variety of notions from statistics and mathematics to acquire good qualitative and quantitative performance. Typically, qualitative performance of these algorithms is measured in terms of visual appearance of the superresolved image, and quantitative performance is measured in terms of peak-signal-to-noise-ratio (PSNR), which is essentially rescaled  $\ell^2$  error. In this context, a superresolution algorithm is considered effective if it results in images with high visual quality and a large PSNR value.

The present article develops an algorithm in the spirit of the second approach, one that is motivated by the rich theory of anisotropic harmonic analysis. We consider a generalization of the state-of-the-art method of superresolution with wavelet sparse mixing estimators (SME). This method was pioneered by Mallat and Yu [16], and has seen strong performance in terms of visual quality and PSNR. Moreover, the motivation for the major aspects of the algorithm are rooted in statistics; the choice of wavelets for the frame in SME is motivated by the efficiency of wavelets for many images. Our generalization incorporates the anisotropic frame of shearlets into this regime, in order to capitalize on the theoretical near-optimality of shearlets for sparsely representing certain images [17, 18]. This algorithm builds on earlier prototypes, in which the use of shearlets and other directional systems allows for improvement over more naive superresolution methods, particularly standard bicubic interpolation methods [19, 20]. The structure of this article is as follows. Section 2 covers background on superresolution. Section 3 covers background on harmonic analysis, and gives a theoretical justification of the use of shearlets in the proposed algorithm. Section 4 details our algorithm. Section 5 provides experimental analysis of the proposed algorithms. Section 6 states conclusions and presents future directions.

## 2. BACKGROUND ON SUPERRESOLUTION

The problem of superresolution is significant in image processing. Mathematically, superresolution is often considered as the recovery of high-frequency components of a signal, given degraded or limited measurements [11, 15, 9].

It can be understood in at least two contrasting ways: as a stand alone problem, or as a recovery problem. The first regime is interested in increasing the resolution of an image as a problem in and of itself; in particular, there is no truth image against which the superresolved image is to be compared. As a recovery problem, superresolution aims to increase the resolution of a downsampled and noisy signal by inverting the operator  $\mathcal{L}$  and denoising  $\mathcal{N}$  as in (1) ; the signal produced by the superresolution algorithm may then be compared to the original image before downsampling and adding noise. Theoretically, this involves inversion; however, the problem (1) is usually ill-posed. For numerical algorithms, interpolation is usually performed instead of true inversion.

In both cases, the goal of superresolution is to increase the resolution of an image  $I$ , while preserving detail and without producing artifacts. The outcome of a superresolution algorithm is an image  $\tilde{I}$ , with the same content as  $I$ , but at a higher resolution. In this theoretical discussion, we restrict ourselves to greyscale images. This allows us to consider our images as real-valued matrices.

Let  $I$  be an  $M \times N$  matrix and  $\tilde{I}$  an  $\tilde{M} \times \tilde{N}$  matrix, with  $M < \tilde{M}$ ,  $N < \tilde{N}$ . We consider the common case where  $\tilde{M} = 2M$  and  $\tilde{N} = 2N$ , which corresponds to doubling the resolution of the original image. Images with multiple channels, such as hyperspectral images, can be superresolved by superresolving each channel separately, perhaps after some form of dimension reduction.

Superresolution can be implemented by using information in addition to  $I$ , such as low resolution images at sub-pixel shifts of the scene [21, 22], or images of the scene with different modalities. The latter method is related to the specific problem of pan-sharpening [23, 24]. In general, the incorporation of additional information sources into the process of superresolution is similar to the approach of image fusion. Alternatively, superresolution can be performed using only  $I$ ; this is called *single-image superresolution*. The first type of superresolution requires additional data, and is thus a more restrictive setting. In this article, we shall develop a single-image superresolution method which requires as input only the image itself.

### 2.1. Isotropic Superresolution Methods

There are several standard approaches to superresolving  $I$  without using additional information such as subpixel shifts. Among the most common are *nearest neighbor interpolation* and *bicubic interpolation*. Let us consider  $\tilde{I} = \{\tilde{a}_{i,j}\}$ , a superresolved version of  $I = \{a_{m,n}\}$ . Here, the values  $\tilde{a}_{i,j}$  and  $a_{m,n}$  may be understood as entries of a real matrix representing the images. We must compute each pixel value in the new image, namely  $\tilde{a}_{i,j}$ , from the pixel values of the original image,  $a_{m,n}$ .

In the case of nearest neighbor interpolation, new pixel values are computed replicating current pixel values. This method is simple and computationally efficient, but leads to extremely jagged superresolved images. It is unsuitable when a high-quality, smooth  $\tilde{I}$  is required. Other methods involve convolving the image with an interpolation kernel, which amounts to taking a weighted average of pixel values within some neighborhood. For example, bicubic interpolation determines  $\tilde{I}$  by computing each  $\tilde{a}_{i,j}$  as a weighted average of the 16 nearest neighbors in  $I$ ; the weights are chosen to approximate the derivative values at the pixels being analyzed [25]. Isotropic interpolation methods using splines have also been studied [26], as have those that emphasize edges [27].

### 2.2. Superresolution with Sparse Mixing Estimators

Beyond such naive interpolation schemes, a variety of more sophisticated superresolution methods abound [28, 29, 30]. One method that has achieved state-of-the-art results is the method of sparse mixing estimators (SME) [16]. This method, pioneered by Mallat and Yu, takes advantage of block sparsity [31] by decomposing the image to be superresolved into a redundant frame, then directionally interpolating based on a sparse frame representation. We outline their basic approach below.

Given a signal  $y$  as in (1), we wish to write  $y$  according to a sparse mixture model. To do this, we consider a family of blocks  $\mathcal{B}$  and a frame  $\Psi$ . The family of blocks may be understood as subsets of the space of all coefficients, in the sense of [31, 32]. Given our signal  $y$ , the coefficients of  $y$  in  $\Psi$  are denoted  $c = \mathcal{F}_\Psi y$ , where  $\mathcal{F}_\Psi$  is the frame operator associated to  $\Psi$ . The synthesis operator is  $\mathcal{F}_\Psi^*$ , so  $\mathcal{F}_\Psi^* c = y$  in the case that  $\Psi$  is a tight frame. We let  $y_B = \mathcal{F}_\Psi^*(c \mathbb{1}_B)$  be the synthesis operator applied only to the block of coefficients  $B$ . Then we seek to write  $y$  of the form:

$$y = \sum_{B \in \mathcal{B}} \tilde{a}(B) y_B + y_r, \quad (2)$$

for a choice of mixing coefficients  $\{\tilde{a}(B)\}_{B \in \mathcal{B}}$  and a residual  $y_r$ . The mixing coefficients determine

how strongly the coefficients from a given block will contribute to the reconstructed signal. The coefficients should be chosen for both fidelity and to promote block sparsity, which will be used to efficiently directionally interpolate the image. With this dual purpose in mind, the coefficients are chosen to satisfy the optimization problem

$$\tilde{a} = \arg \min_a \frac{1}{2} \left\| c \left( 1 - \sum_{B \in \mathcal{B}} a(B) \mathbb{1}_B \right) \right\|_2^2 + \lambda \sum_{B \in \mathcal{B}} |a(B)| \|\bar{R}_B c\|_B^2,$$

where  $\|\cdot\|_B^2$  is the squared  $L^2$  norm on the block  $B$ . The first term is a typical fidelity term, in this case an  $\ell^2$ -error minimizing term, while the second term enforces block sparsity according to the  $\|\bar{R}_B c\|_B^2$  factor. These factors are regularizers that approximate the energy of the frame coefficient variations relative to their average in the direction of the block  $B$ . If  $\|\bar{R}_B c\|_B^2$  is small, then there is a strong degree of directional regularity present in the block, which can be exploited. Such blocks are favored in the present regime. In practice, for a block oriented at angle  $\theta$ ,

$$\bar{R}_B c = c|_B - \bar{c}|_B,$$

where,  $\bar{c}(k, j) =$  average of the  $k^{th}$  frame coefficients in block  $B$  located on the line passing through  $j$ , at angle  $\theta$ , where  $k$  runs through all frame coefficients. For example, if  $\Psi$  is a single level 2- $D$  discrete wavelet transform, as is the case in [16], then  $k = 1, 2, 3$ , corresponding to the vertical, horizontal, and diagonal components of the high pass aspect of the wavelet frame. The fidelity and sparsity components are balanced by a tunable parameter  $\lambda$ .

The signal of interest,  $f$ , is then approximated by exploiting the decomposition (2). Let  $\mathcal{B}_\theta$  be the blocks oriented in the direction  $\theta$ , so that  $\mathcal{B} = \bigcup_\theta \mathcal{B}_\theta$ . Let  $U_\theta^+$  be a directional interpolator in the direction  $\theta$ , and  $U^+$  an isotropic interpolator. We estimate  $f$  as

$$\tilde{f} = U^+ y + \sum_\theta (U_\theta^+ - U^+) \tilde{\Psi} \left( \sum_{B \in \mathcal{B}_\theta} \tilde{a}(B) \mathbb{1}_B c \right).$$

The aim of this paper is to develop a superresolution algorithm that computes dominant directions efficiently and accurately, using the harmonic analytic construction of *shearlets* [33, 34, 17, 35]. This

method is quite general, can be applied to images of any size, and has few tunable parameters. Moreover, shearlets are known to provide near-optimally sparse representations for a certain class of signals, known as cartoon-like signals. This property suggests their use in many applications in which wavelets are known to provide strong performance. Indeed, our approach has some similarities with morphological signal analysis [36], which has been used for superresolution in a different context [37].

### 3. BACKGROUND ON HARMONIC ANALYSIS

This section provides mathematical background on harmonic analysis, in particular the basics of wavelet and shearlet constructions. This will motivate the use of shearlets in our superresolution algorithm.

#### 3.1. Background on wavelet theory

Shearlets are a generalization of wavelets that incorporates a notion of directionality. We thus begin our mathematical discussion of shearlets with some background on wavelets [38, 39].

In a broad sense, wavelet algorithms decompose an image with respect to *scale* and *translation*. Mathematically, given a signal  $f \in L^2([0, 1]^2)$ , understood as an ideal image signal, and an appropriately chosen wavelet function  $\psi$ ,  $f$  may be written as

$$f = \sum_{m \in \mathbb{Z}} \sum_{n \in \mathbb{Z}^2} \langle f, \psi_{m,n} \rangle \psi_{m,n}, \quad (3)$$

where:

- $\psi_{m,n}(x) := |\det A|^{m/2} \psi(A^m x - n)$ .
- $A \in GL_2(\mathbb{R})$ .

A typical choice for  $A$  is the dyadic isotropic matrix

$$A = \begin{pmatrix} 2 & 0 \\ 0 & 2 \end{pmatrix}.$$

The set of wavelet coefficients  $\{\langle f, \psi_{m,n} \rangle\}_{m \in \mathbb{Z}, n \in \mathbb{Z}^2}$  describes the behavior of  $f$ , our image signal, at different scales (determined by  $m$ ) and at different translations (determined by  $n$ ). This infinite

scheme is truncated to work with real, finite image signals [40]. Wavelets have been effectively applied to problems in image compression [41], image fusion [42], and image registration [43].

There are a variety of implementations of wavelets in many programming languages. Discrete wavelet transforms offer great flexibility in choice of  $\psi$ , and filterbank implementations enjoy many geometric invariance properties, and also low computational complexity. Indeed, filterbank wavelet implementations have computational complexity of  $O(N^2)$  for an  $N \times N$  image. They are also known to provide sparser representations of an image, when compared with Fourier methods [44].

### 3.2. Background on shearlet theory

Beginning in the early 2000s, several efforts were made to extend wavelet theory to be *anisotropic*, that is, to include a directional character in the coefficients it produces. Among the most prominent of these theoretical constructions are curvelets [45], contourlets [46], and shearlets [17, 34]. Shearlets generalize wavelets by decomposing with respect not just to *scale* and *translation*, but also *direction*. Mathematically, given a signal  $f \in L^2([0, 1]^2)$  and an appropriate shearlet function  $\psi$ , we may decompose  $f$  as

$$f = \sum_{i \in \mathbb{Z}} \sum_{j \in \mathbb{Z}} \sum_{k \in \mathbb{Z}^2} \langle f, \psi_{i,j,k} \rangle \psi_{i,j,k}, \quad (4)$$

where:

- $\psi_{i,j,k}(x) := 2^{\frac{3i}{4}} \psi(B^j A^i x - k).$
- $A = \begin{pmatrix} 2 & 0 \\ 0 & 2^{\frac{1}{2}} \end{pmatrix}, B = \begin{pmatrix} 1 & 1 \\ 0 & 1 \end{pmatrix}.$

Note that  $A$  is no longer isotropic, hence it will allow our new analyzing functions to be more pronounced in a particular direction. The new matrix  $B$ , a shearing matrix, lets us select the direction. The shearlet coefficients  $\{\langle f, \psi_{i,j,k} \rangle\}_{i,j \in \mathbb{Z}, k \in \mathbb{Z}^2}$  describe the behavior of  $f$  at different scales (determined by  $i$ ), translations (determined by  $k$ ) and directions (determined by  $j$ ). Higher dimensional generalizations of this construction exist as well [47, 48, 49].

The anisotropic character of shearlets has proven useful for a variety of problems in image processing, including image denoising [50], image registration [51], inpainting, [52], and image fusion [53]. Preliminary results of the superresolution of images using shearlets have been reported [19]. The ambition

of this article is to further study the role of anisotropic harmonic analysis in the problem of image superresolution, by more efficiently utilizing the sparsity afforded by the shearlet representation.

### 3.3. Shearlets for Optimal Representation

From a theoretical standpoint, shearlets near-optimally resolve  $\mathcal{C}^2$  boundaries [17, 18]. More precisely, shearlet frames provide near-optimally sparse representations of *cartoon-like images* [54]:

**Definition 3.1.** The set of *cartoon-like images* in  $[0, 1]^2$  is

$$\mathcal{E} := \{f \mid f = f_0 + \chi_B f_1, f_i \in \mathcal{C}^2([0, 1]^2), \|f_i\|_{\mathcal{C}^2} \leq 1, B \subset [0, 1]^2, \partial B \in \mathcal{C}^2([0, 1])\}.$$

The space of cartoon-like images is a quantitative definition of continuous signals that represent certain real images. That is, although real images are discrete, if we are to consider only continuous signals, then  $\mathcal{E}$  represents the class of continuous signals corresponding to images consisting of smooth edges and discontinuities. Intuitively, signals in  $\mathcal{E}$  are smooth except along boundaries of smooth curves.

**Theorem 3.2.** [17] *Let  $f \in \mathcal{E}$ , and let  $f_N^W, f_N^S$  be the best  $N$ -term approximations to  $f$  in a wavelet system and shearlet system, respectively. Then these approximations satisfy the following sharp bounds, for some fixed constant  $C > 0$ :*

$$\begin{aligned} \|f - f_N^W\|_2^2 &\leq CN^{-1} \\ \|f - f_N^S\|_2^2 &\leq CN^{-2}(\log(N))^3. \end{aligned}$$

The improved sparsity of shearlet systems, compared to wavelet systems, suggests the role of shearlets in the SME superresolution regime. Indeed, the goal of this regime is to efficiently represent an image signal in a block sparse way, in order to extract pertinent directional information that can then be adaptively interpolated. By decomposing in a shearlet frame, rather than a wavelet frame, we bring this improved sparsity to bear on the problem of superresolution. This is of course motivated by the fact that many images of interest fall into the cartoon-like regime [54].

### 3.4. Fast Finite Shearlet Transform

Since the advent of shearlets, several numerical schemes have been proposed. The ShearLab implementation [55] offers the most flexibility, and has the benefit of being partially coded in C, leading to



faster runtime on large images. The fast finite shearlet transform (FFST) [56], on the other hand, is very intuitive, and is coded entirely in MATLAB. We note that a GPU implementation of shearlets has also been proposed [57].

The FFST is in some ways the most intuitive implementation of the shearlet transform, and is the implementation deployed for our algorithm. ShearLab implementations were also considered, with little change in performance. We start by constructing a generating shearlet in the frequency domain  $\hat{\psi} : \mathbb{R}^2 \rightarrow \mathbb{R}$ , which satisfies the *classical shearlet* assumption:

$$\hat{\psi}(\omega) = \hat{\psi}(\omega_1, \omega_2) = \hat{\psi}_1(\omega_1) \hat{\psi}_2\left(\frac{\omega_2}{\omega_1}\right), \quad \hat{\psi}_i : \mathbb{R} \rightarrow \mathbb{R}.$$

This property is convenient for proving the corresponding shearlet systems is actually a frame. Note that  $\hat{f}$  denotes the Fourier transform of  $f$  [58].

Define a function  $b : \mathbb{R} \rightarrow \mathbb{R}$  by

$$b(\omega) := \begin{cases} \sin(\frac{\pi}{2}v(|\omega| - 1)) & \text{for } 1 \leq |\omega| \leq 2, \\ \cos(\frac{\pi}{2}v(\frac{1}{2}|\omega| - 1)) & \text{for } 2 < |\omega| \leq 4, \\ 0 & \text{otherwise,} \end{cases}$$

where  $v$  is defined by

$$v(x) := \begin{cases} 0 & \text{for } x < 0, \\ 35x^4 - 84x^5 + 70x^6 - 20x^7 & \text{for } 0 \leq x \leq 1, \\ 1 & \text{for } x > 1, \end{cases} \quad (5)$$

as in the Meyer wavelet. Then,  $\psi_1$  is given in the frequency domain by

$$\hat{\psi}_1(\omega) := \sqrt{b^2(2\omega) + b^2(\omega)}.$$

It can be shown that  $\text{supp}(\hat{\psi}_1) = [-4, -\frac{1}{2}] \cup [\frac{1}{2}, 4]$  and that

$$\sum_{j \geq 0} |\hat{\psi}_1(2^{-2j}\omega)|^2 = 1 \quad \text{for } |\omega| > 1.$$

Next,  $\psi_2$  is defined by

$$\hat{\psi}_2(\omega) := \begin{cases} \sqrt{v(1+\omega)} & \text{for } \omega \leq 0, \\ \sqrt{v(1-\omega)} & \text{for } \omega > 0. \end{cases}$$

This function has support  $[-1, 1]$  and satisfies:

$$\sum_{k=-1,0,1} |\hat{\psi}_2(k+\xi)|^2 = 1 \quad \text{for } \xi \in [-1, 1]. \quad (6)$$

The FFST uses a modified form of cone-adapted shearlets [54], where the frequency domain is divided into four non-disjoint sets:

$$\begin{aligned} \mathcal{C}^0 &:= \{(\omega_1, \omega_2) \in \mathbb{R}^2 : |\omega_1| < 1, |\omega_2| < 1\}, \\ \mathcal{C}^h &:= \{(\omega_1, \omega_2) \in \mathbb{R}^2 : |\omega_2/\omega_1| < 1, |\omega_1| \geq 1/2\}, \\ \mathcal{C}^v &:= \{(\omega_1, \omega_2) \in \mathbb{R}^2 : |\omega_1/\omega_2| < 1, |\omega_2| \geq 1/2\}, \\ \mathcal{C}^\times &:= \{(\omega_1, \omega_2) \in \mathbb{R}^2 : |\omega_1| \geq 1/2, |\omega_2| \geq 1/2, |\omega_1| = |\omega_2|\}. \end{aligned}$$

The open square  $\mathcal{C}^0$  is the low-pass region; it captures information that exists at low frequencies. The cones  $\mathcal{C}^h$  and  $\mathcal{C}^v$  partition the frequency plane into horizontally and vertically oriented cones, respectively. The last region,  $\mathcal{C}^\times$ , represents the intersection of the horizontal and vertical cones. We also note that  $\mathcal{C}^0$  now intersects non-trivially with both cones. This allows our shearlets to transition more smoothly across region boundaries. We address each region in turn by defining the generating shearlet.

For the low-pass region,  $\mathcal{C}^0$ , we use the Meyer scaling function, whose Fourier transform is given by

$$\hat{\varphi}(\omega) := \begin{cases} 1 & \text{for } |\omega| \leq 1/2, \\ \cos(\frac{\pi}{2}v(2|\omega| - 1)) & \text{for } 1/2 < |\omega| < 1, \\ 0 & \text{otherwise,} \end{cases}$$

to define the full scaling function

$$\hat{\phi}(\omega_1, \omega_2) := \begin{cases} \varphi(\omega_1) & \text{for } |\omega_2| \leq |\omega_1|, \\ \varphi(\omega_2) & \text{for } |\omega_1| < |\omega_2|. \end{cases}$$

For  $\mathcal{C}^h$  and  $\mathcal{C}^v$ , we use

$$\begin{aligned}\hat{\psi}^h(\omega_1, \omega_2) &= \hat{\psi}_1(\omega_1) \hat{\psi}_2\left(\frac{\omega_2}{\omega_1}\right), \\ \hat{\psi}^v(\omega_1, \omega_2) &= \hat{\psi}_1(\omega_2) \hat{\psi}_2\left(\frac{\omega_1}{\omega_2}\right).\end{aligned}$$

Finally, for  $\mathcal{C}^\times$ ,  $\hat{\psi}^h = \hat{\psi}^v$  and we use the common values to define  $\hat{\psi}^x$  there.

Now, let  $f$  be an  $M \times N$  image, considered as a function on the grid  $\mathcal{G} := \{(m_1/M, m_2/N) : m_1 = 0, \dots, M-1, m_2 = 0, \dots, N-1\}$  with periodic extension. Define  $j_0 := \lfloor \log_2 \max\{M, N\} \rfloor$ . We discretize the shearlet parameters in (4) as follows:

$$\begin{aligned}a_j &:= 2^{-2j} = \frac{1}{4^j}, \quad j = 0, \dots, j_0 - 1, \\ s_{j,k} &:= k 2^{-j}, \quad -2^j \leq k \leq 2^j, \\ t_m &:= \left(\frac{m_1}{M}, \frac{m_2}{N}\right), \quad m \in \mathcal{G}.\end{aligned}$$

Our shearlets then are given by

$$\psi_{j,k,m}^\kappa(x) := \psi_{a_j, s_{j,k}, t_m}^\kappa = \psi^\kappa(A_{a_j}^{-1} S_{s_{j,k}}^{-1}(x - t_m)), \quad \kappa = h, v.$$

With this choice of parameters, the shearlets have support entirely within one of the cones, except for  $|k| = 2^j$ . In this case, the shearlets in both cones agree, so we can choose either function, which we will call  $\psi^{h \times v}$ . The low-pass region is handled by translations of the full scaling function:  $\phi_t(x) := \phi(x - t)$ . One can calculate simple formulas for the shearlet coefficients. For instance, in the horizontal cone, we have

$$\begin{aligned}\mathcal{SH}(f)(j, k, m) &= \langle f, \psi_{j,k,m}^h \rangle \\ &= \langle \hat{f}, \hat{\psi}_{j,k,m}^h \rangle \\ &= \mathcal{F}^{-1}(\hat{f}(\omega_1, \omega_2) \hat{\psi}(4^{-j}\omega_1, 4^{-j}k\omega_1 + 2^{-j}\omega_2))\end{aligned}$$

where  $\omega_1 = -\lfloor M/2 \rfloor, \dots, \lceil M/2 \rceil - 1$ ,  $\omega_2 = -\lfloor N/2 \rfloor, \dots, \lceil N/2 \rceil - 1$ . The Fourier transforms and inverse Fourier transforms are to be interpreted as discrete Fourier transforms, and hence can be implemented by 2-D FFTs. After a lengthy and technical series of calculations, it can be shown that

the shearlets form a Parseval frame for  $L^2(\mathcal{G})$ .

**Theorem 3.3** (Theorem 3.1, [59]). *The discrete shearlet system*

$$\begin{aligned} & \{\psi_{j,k,m}^h(x) : j = 0, \dots, j_0 - 1, -2^j + 1 \leq k \leq 2^j - 1, m \in \mathcal{G}\} \\ & \cup \{\psi_{j,k,m}^v(x) : j = 0, \dots, j_0 - 1, -2^j + 1 \leq k \leq 2^j - 1, m \in \mathcal{G}\} \\ & \cup \{\psi_{j,k,m}^{h \times v}(x) : j = 0, \dots, j_0 - 1, |k| = 2^j, m \in \mathcal{G}\} \\ & \cup \{\phi_m(x) : m \in \mathcal{G}\} \end{aligned}$$

*forms a Parseval frame for  $L^2(\mathcal{G})$ .*

We note that both the ShearLab and FFST implementations of shearlets are based on the fast Fourier transform, and consequently have computational complexity of  $O(N^2 \log N)$  for an  $N \times N$  image. So, shearlets are more computationally complex than wavelets, but only by a logarithmic factor.

### 3.5. Directional Identification with Numerical Shearlets

In addition to offering near-optimal sparsity properties for cartoon-like images, shearlets have a strong directional nature. The structure of discrete shearlet systems is readily employed to identify edge location and orientation; this information can be incorporated into the adaptive directional interpolation portion of a superresolution algorithm. To put this in the context of a concrete superresolution problem, we consider the simple example of angled half-planes. To do so, we perform a few basic calculations related to the FFST. These results indicate that the FFST effectively identifies both the existence of such singularities, and their orientation. In the context of image processing, this means the FFST is well-suited for resolving edges; we make use of this efficiency in our proposed superresolution algorithm. Some of these calculations are adapted from [60]. A full exposition of the following arguments are in [61]

**Lemma 3.4.** *Let  $\psi \in S(\mathbb{R}^2)$ ,  $r \in \mathbb{R}$ . Then*

$$\int_{\mathbb{R}} \hat{\psi}(-r\omega, \omega) d\omega = \int_{\mathbb{R}} \psi(x, rx) dx.$$

*Proof.* Define  $f(y) = \int_{\mathbb{R}} \psi(x, y + rx) dx$ .

$$\begin{aligned}
\int_{\mathbb{R}} \hat{\psi}(-r\omega, \omega) d\omega &= \int_{\mathbb{R}} \int_{\mathbb{R}^2} \psi(x, y) e^{-2\pi i(-rx+y)\omega} dx dy d\omega \\
&= \int_{\mathbb{R}} \int_{\mathbb{R}} \int_{\mathbb{R}} \psi(x, y' + rx) e^{-2\pi i y' \omega} dy' dx d\omega \\
&= \int_{\mathbb{R}} \int_{\mathbb{R}} f(y) e^{-2\pi i y \omega} dy d\omega \\
&= \int_{\mathbb{R}} \hat{f}(\omega) d\omega \\
&= f(0) \\
&= \int_{\mathbb{R}} \psi(x, rx) dx.
\end{aligned}$$

□

Let  $H_{y>rx}$  denote the characteristic function of the half-plane

$$\{(x, y) \in \mathbb{R}^2 | y > rx\},$$

for some fixed  $r \in \mathbb{R}$ . Let  $f_{x_i} = \frac{\partial f}{\partial x_i}$ .

**Lemma 3.5.**

$$\frac{\partial}{\partial y} H_{y>rx} = \delta_{y-rx}$$

in the sense of distributions.

*Proof.* Let  $\psi \in C_c^\infty(\mathbb{R}^2)$ .

$$\begin{aligned}
\langle \frac{\partial}{\partial y} H_{y>rx}, \psi \rangle &= -\langle H_{y>rx}, \psi_y \rangle \\
&= -\int_{\mathbb{R}^2} H_{y>rx} \psi_y dx dy \\
&= -\int_{-\infty}^{\infty} \int_{rx}^{\infty} \psi_y dy dx \\
&= \int_{\mathbb{R}} \psi(x, rx) dx \\
&= \langle \delta_{y-rx}, \psi \rangle.
\end{aligned}$$

□

**Lemma 3.6.**

$$\widehat{H_{y>rx}} = \frac{1}{2\pi i \omega_2} \widehat{\delta_{y-rx}},$$

in the sense of distributional Fourier transforms, where  $\widehat{\delta_{y-rx}}$  acts by

$$\langle \widehat{\delta_{y-rx}}, \hat{\psi} \rangle = \int_{\mathbb{R}} \hat{\psi}(-r\omega, \omega) d\omega, \quad \hat{\psi} \in C_c^\infty(\mathbb{R}^2).$$

*Proof.* Note that  $\widehat{\delta_{y-rx}} = \frac{\partial}{\partial y} \widehat{H_{y>rx}} = (2\pi i \omega_2) \widehat{H_{y>rx}}$  so the first claim follows. For the second claim, we use Parseval's identity and Lemma 3.4:

$$\begin{aligned} \langle \widehat{\delta_{y-rx}}, \hat{\psi} \rangle &= \langle \delta_{y-rx}, \psi \rangle \\ &= \int_{\mathbb{R}} \psi(x, rx) dx \\ &= \int_{\mathbb{R}} \hat{\psi}(-r\omega, \omega) d\omega. \end{aligned}$$

□

We can now prove that shearlets, as implemented by the FFST, efficiently detect the direction of discontinuities in half-planes.

**Theorem 3.7.** *Discretize the position, dilation, and shear parameters and define  $\psi$  as in the FFST. Assume without loss of generality that  $|r| \leq 1$ . Let  $f(x, y) = H_{y>rx}$  and fix a scale  $j$  and position  $m$ . For almost all values of  $r$ , the shearlet transform of  $f$ ,  $\mathcal{SH}(f)(j, k, m)$ , is only non-zero for two consecutive values of the shearing parameter  $k$ . These values satisfy*

$$|s_{j,k} - r| < \frac{1}{2^j}.$$

*Furthermore, for the unique  $k$  that maximizes  $|\mathcal{SH}(f)(j, k, m)|$ ,  $s_{j,k}$  is closest to  $r$  over all  $k$ .*

*Proof.*

$$\begin{aligned}
\mathcal{SH}(f)(j, k, m) &= \langle f, \psi_{j,k,m} \rangle \\
&= \langle \hat{f}, \hat{\psi}_{j,k,m} \rangle \\
&= \int_{\mathbb{R}^2} \frac{1}{2\pi i \omega_2} \widehat{\delta_{y-rx}}(\omega_1, \omega_2) \hat{\psi}_{j,k,m}(\omega_1, \omega_2) d\omega_1 d\omega_2 \\
&= \frac{1}{2\pi i} \int_{\mathbb{R}} \frac{1}{\omega_2} \hat{\psi}_{j,k,m}(-r\omega_2, \omega_2) d\omega_2.
\end{aligned}$$

By the assumption on  $r$ , we are utilizing the vertical cone, hence

$$\hat{\psi}_{j,k,m}(-r\omega_2, \omega_2) = \hat{\psi}_1(4^{-j}\omega_2) \hat{\psi}_2(-2^j r + k) e^{-2\pi i(-r\omega_2 m_1/M + \omega_2 m_2/N)}.$$

We note that  $k$  only occurs in  $\hat{\psi}_2(-2^j r + k)$ , so maximizing this term will maximize  $|\mathcal{SH}(f)(j, k, m)|$ . The function  $\hat{\psi}_2$  is a non-negative, smooth function supported on  $[-1, 1]$  that is strictly increasing on  $[-1, 0]$  and strictly decreasing on  $[0, 1]$ . The support assumption implies that the term is 0 unless  $-1 < -2^j r + k < 1$ , or equivalently,  $|s_{j,k} - r| < \frac{1}{2^j}$ . Since the shearlets' slopes differ by  $1/2^j$ , this occurs for two consecutive values of  $k$ , except in the case when  $r$  and a shearlet's slope are exactly equal. Here, only one value of  $k$  leads to a non-zero shearlet coefficient. Furthermore, the above term will be maximized when  $-2^j r + k$  is closest to 0, or when  $r$  is closest to  $\frac{k}{2^j} = s_{j,k}$ , the slope of the shearlet's center. There is a unique such  $k$ , unless  $r$  is equidistant between two shearlet directions. Here, two values of  $k$  give identical shearlet coefficients. This completes the proof when  $|r| \leq 1$ . A symmetric argument, using the definition of  $\psi$  in the horizontal cone, shows the result for  $|r| > 1$ .  $\square$

This theorem implies shearlets find the orientation of a simple linear discontinuity very efficiently; this property makes them well-suited to superresolution, where edge resolution is a central problem.

#### 4. Description of Algorithm

In this section, we detail our algorithm. Given an image  $I$  to be superresolved, our algorithm proceeds as follows.

1. Decompose  $I$  in a redundant shearlet frame to acquire coefficients  $c = \mathcal{SH}(I)$ . This is implemented by the FFST [56, 59], but other shearlet algorithms could be considered. To make a consistent comparison with the wavelet-based method of Mallat and Yu, one level of shearlet

decomposition is used.

2. Define a set of blocks  $\mathcal{B}$ . This set is generated from a set of basic blocks, which are then rotated and translated throughout the image. For comparative purposes, the same set of basic blocks and angles as in Mallat and Yu's wavelet-based algorithm are used. The basic blocks consist of 28 anisotropic rectangles of various lengths and area between 12 and 18. The set of angles by which these blocks are rotated consists of 20 equally spaced angles, i.e.  $\{\theta\} = \{\frac{k\pi}{10}\}_{k=1}^{20}$ . More angles could be included, to cover significant directional phenomena that are missed by the current set-up. This would be an issue only for very large images; the largest image analyzed presently is  $512 \times 512$ . The blocks are translated by single pixels in the  $x$  and  $y$  directions throughout the image.

We note that the rotations of the blocks will allow for many edges to be isolated, which exploits the theory developed in Section 3.

3. Compute mixing weights  $\{\tilde{a}(B)\}_{B \in \mathcal{B}}$  according to the representation of  $I$  in the shearlet domain by a mixed  $\ell_2/\ell_1$  minimization:

$$\tilde{a} = \arg \min_a \frac{1}{2} \left\| c \left( 1 - \sum_{B \in \mathcal{B}} a(B) \mathbb{1}_B \right) \right\|_2^2 + \lambda \sum_{B \in \mathcal{B}} |a(B)| \|\bar{R}_B c\|_B^2,$$

where the directional regularization factor is given by

$$\bar{R}_B c = c|_B - \bar{c}|_B.$$

Here,  $\bar{c}|_B(k, j) = \text{average of the } k^{\text{th}} \text{ frame coefficients in } B \text{ located on the line passing through } j, \text{ at angle } \theta$ , where  $k$  runs through all the shearlet coefficients.

4. Directional interpolators  $\{U_\theta^+\}_\theta$  and a bicubic spline interpolator  $U^+$  are applied according to the mixing estimator as:

$$\tilde{I} = U^+ y + \sum_\theta (U_\theta^+ - U^+) \mathcal{S} \mathcal{H}^{-1} \left( \sum_{B \in \mathcal{B}_\theta} \tilde{a}(B) \mathbb{1}_B c \right).$$



Details on the exact construction of the directional interpolators are in [16].

## 5. Experiments and Analysis

To test our proposed algorithm, we consider three classes of images: synthetic images that fall into the cartoon-like regime, real remotely sensed images [62, 63], and standard examples from image processing databases [64, 65]. We selected these images to evaluate the robustness of our algorithm, and test our claim that using shearlets for images with significant directional component (such as that present in cartoon-like imagery) can improve performance over isotropic, wavelet-based methods.

On the one hand, synthetic images provide the most clear benchmark for evaluation of the impact of directionality on superresolution’s performance. On the other hand, however, most images do not fall entirely under either the cartoon-like or the textural regime. They can have aspects that are strongly directional, and aspects that are highly textured. Thus, studying real images from [62, 63] and [64, 65] is important to understanding how the use of directionally-sensitive representation affects our algorithm.

For all our test images, we analyze the quality of the superresolved images produced by the algorithms under comparison from both the qualitative and quantitative standpoint. This is done via visual inspection and computation of peak signal to noise ratio (PSNR). PSNR between two images  $I, \tilde{I}$  is computed with the formula:

$$PSNR(I, \tilde{I}) = -10 \log_{10} \left( \frac{\|I - \tilde{I}\|_2^2}{M * N} \right),$$

where  $I, \tilde{I}$ , are size  $M \times N$ . We note that all images we consider have been converted to grayscale, so that the maximum pixel value is 1 and the minimal pixel value is 0. This requires  $I, \tilde{I}$  to be of the same size. Consequently, the method by which we incorporate PSNR as a measure of superresolution quality is to first degrade  $I$  by first downsampling by a factor of 2, then possibly adding some combination of Gaussian convolutional blur and Gaussian noise, to get  $I_d$ . A superresolution algorithm is then applied to  $I_d$  to acquire  $\tilde{I}$ . A high value of RMSE indicates a good superresolution performance.

We consider four algorithms for superresolution: cubic spline linear interpolation [16], shearlet blurring [19, 66, 67], SME with wavelets [16], and our proposed method, namely SME with shearlets. The shearlet blurring method identifies directed edges with the shearlet transform, then smoothes out

discontinuities generated from bicubic interpolation by blurring locally in these directions.

In addition, four choices of degradation operator are considered: downsampling, downsampling combined with blurring, downsampling combined with adding Gaussian white noise, and downsampling combined with blurring and adding Gaussian white noise. Each degradation operator is evaluated separately. All code and experimental evaluation is in MATLAB.

### 5.1. Data for Experiments

We began by testing our shearlet SME algorithm on synthetically generated images of simple geometric objects. We present three in the present article: a half-plane of slope 5, a circle, and a parabola. These images, which appear in Figure 1, are binary: one part of the image has value 1, the other value 0. These images were chosen because they illustrate images that are extremely smooth (in fact, constant) away from a  $C^2$  discontinuity. These discontinuities are smooth, corresponding to linear, circular, and quadratic discontinuities, respectively. The theory of shearlets for resolving edges suggests these images will be well-captured in a shearlet frame, and thus the shearlet SME algorithm ought to perform well.

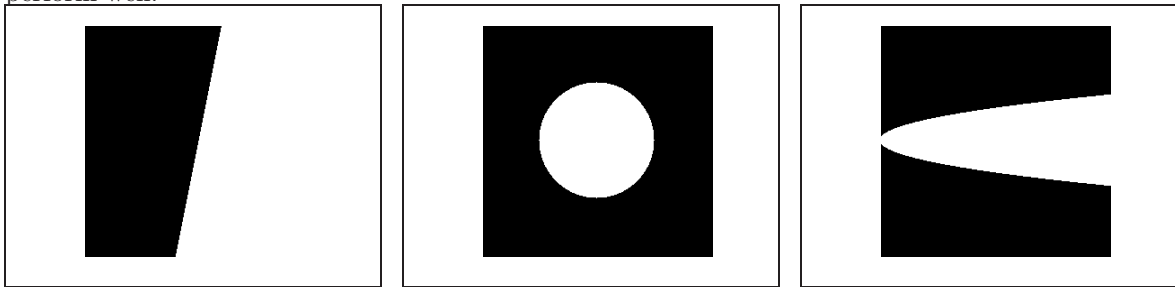


**Figure 1:** *Synthetic images for superresolution algorithm evaluation, from left to right: half plane, circle, parabola. These simple images fit easily into the cartoon-like regime, and should give some indication of if the basic premise of the proposed algorithm is tenable. Indeed, the proposed algorithm is based on using shearlets, due to their near-optimality in sparsely representing cartoon-like images. All synthetic images are of size  $256 \times 256$ .*

We next consider real remotely sensed images of different modalities. In the field of remote sensing, airborne and spaceborne satellites record information at various frequencies, resolutions, and modalities, which are then interpreted by scientists and engineers for environmental analysis. There is a great variety in these images; we consider three in Figure 2. These images contain both edge and textural features. They thus represent a realistic test of our algorithm, especially in light of the importance of superresolution in remote sensing [5, 6, 7, 8].

The last images considered presently are three from the standard image processing library. As with the remotely sensed images, these images do not fall in the cartoon-like regime, where shearlets are

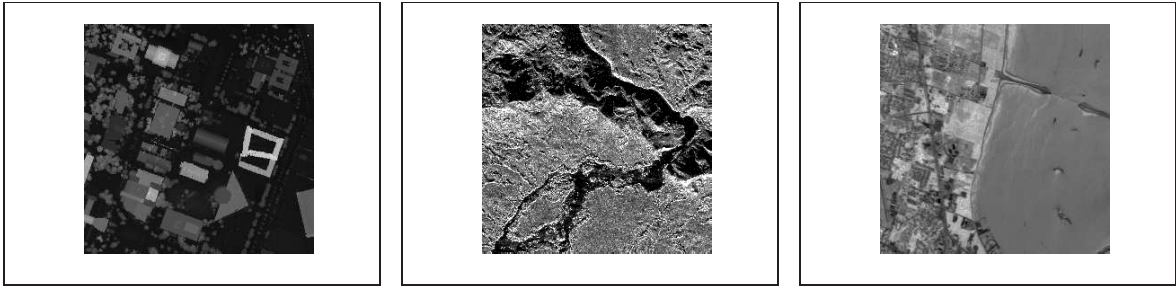


**Figure 2:** Remotely sensed images for superresolution evaluation, from left to right: lidar, synthetic aperture radar (SAR), and a single band of a hyperspectral image (HSI). The lidar scene is courtesy of the IEEE GRSS data fusion contest [63]. The SAR scene is courtesy of David J. Harding of the NASA Goddard Space Flight Center. The hyperspectral image is of the NASA Kennedy Space Flight Center, and can be found at [62]. Unlike the synthetic examples, these images do not fall entirely in the cartoon-like regime. Indeed, these images are a more complicated combination of edges and textures. All images are of size  $256 \times 256$ .

known to perform near-optimally with respect to sparsity. Instead, these images have sharp edges, subtle textures, and oscillating patterns.



**Figure 3:** Image processing standard library for superresolution evaluation, from left to right: peppers, cameraman, mandrill. Peppers and mandrill may be found at [65], and cameraman may be found at [64]. Like the remotely sensed images, these images contain both cartoon-like and textural features. Peppers and mandrill are  $512 \times 512$ , while cameraman is  $256 \times 256$ .

We note that we also considered images on which shearlets are not known to perform near-optimally: textures. For these images, curvelets have been proved to be suboptimal [68]. Curvelets and shearlets have similar properties for representing cartoon-like images, which suggests shearlets will be suboptimal for textures as well. The results on these images tended to favor wavelet methods, which is unsurprising. Indeed, the cartoon-like structure shearlets optimize is not present in such images.

## 5.2. Experiments with Downsampling

The most straightforward evaluation of our method considered was a degradation operator that simply downsamples the image. For these experiments, and all subsequent experiments, we downsampled by a factor of 2.

Our results indicate that shearlet SME outperforms all other methods, including SME with wavelets.

Image	linear	shearlet blur	SME wavelet	SME shearlet
plane	29.3764	27.2592	31.5270	<b>32.7195</b>
circle	28.8725	27.9372	29.9733	<b>30.3056</b>
parabola	26.4058	25.5372	28.2656	<b>28.9741</b>
lidar	27.4732	26.1318	28.2076	<b>28.3089</b>
SAR	13.6952	13.7526	14.1380	<b>14.2107</b>
HSI	33.1773	31.5585	33.5233	<b>33.5956</b>
peppers	17.0726	16.4935	17.6425	<b>17.7495</b>
cameraman	24.9684	23.4964	25.7850	<b>26.0223</b>
mandrill	21.7236	20.5117	22.2289	<b>22.3394</b>

**Table 1:** *The PSNR values for experiments involving downsampling only. Without exception, SME shearlets gives the best performance, with particularly strong results for the synthetic examples and cameraman. This is in correspondence with the theory of shearlets, since these images are arguably the most cartoon-like of the images analyzed.*

In particular, the PSNR results of shearlet SME on the synthetic examples and cameraman are substantial. Given that these images are rather cartoon-like, compared to some of the remotely sensed images, for example, this makes sense. Indeed, the more cartoon-like an image is, the more we would expect our algorithm to outperform SME with wavelets. We note also that the shearlet blurring method performs poorly in general, out performing linear cubic spline interpolation only for the noisy synthetic aperture radar image. This could be due to the fact that the blurring method tends to smooth out noise, which could be relatively useful for such noisy images.

### 5.3. Experiments with Downsampling and Blurring

We next considered a degradation operator of downsampling by a factor of 2, then applying an isotropic Gaussian blur. The blur is implemented by applying a low-pass Gaussian blur of size  $3 \times 3$  and standard deviation  $\sigma = .5$  to the already downsampled image. This is a more complicated inverse problem in the sense of (1) than mere downsampling.

Our results show a slightly worse performance than when the degradation operator was downsampling alone. Indeed, shearlet SME gives the best performance in only 7/9 experiments, as opposed to 9/9 in the case of downsampling alone. This is possibly due to the softening of edges, wrought by the Gaussian convolutional blur. Indeed, as the edges become blurrier, the benefits of shearlets tend to diminish. Still, performance is overall good, particularly on the synthetic examples.

Image	linear	shearlet blur	SME wavelet	SME shearlet
plane + blur	29.2262	27.0262	30.3043	<b>30.9394</b>
circle + blur	28.9828	27.6524	29.4787	<b>29.6421</b>
parabola + blur	26.5469	25.3089	27.5883	<b>28.0918</b>
lidar + blur	27.6199	26.2680	<b>27.7956</b>	27.7366
SAR + blur	14.3770	14.0051	14.5165	<b>14.5579</b>
HSI + blur	33.0303	31.6975	<b>32.9434</b>	32.9067
peppers + blur	17.5671	16.5422	17.7788	<b>17.8298</b>
cameraman + blur	24.7660	23.3046	25.0483	<b>25.1635</b>
mandrill + blur	21.9427	20.8192	22.0670	<b>22.1136</b>

**Table 2:** The PSNR values for experiments involving downsampling and blurring. The results are less impressive than for downsampling alone, possibly due to the softening of edges caused by applying the Gaussian convolutional blur.

#### 5.4. Experiments with Downsampling and Noise

The next degradation operator considered was downsampling by a factor of 2, then adding Gaussian white noise. The Gaussian noise was of mean  $\mu = 0$  and standard deviation  $\sigma = .1$ .

Image	linear	shearlet blur	SME wavelet	SME shearlet
plane + noise	22.7296	22.5127	23.4328	<b>23.6691</b>
circle + noise	22.5808	22.6856	23.1614	<b>23.2911</b>
parabola + noise	22.0640	21.9982	22.8920	<b>23.1531</b>
lidar + noise	20.9147	21.4511	21.6273	<b>21.7589</b>
SAR + noise	13.1773	13.4748	13.6335	<b>13.6936</b>
HSI + noise	22.3581	22.9443	23.0341	<b>23.1390</b>
peppers + noise	16.4586	16.0813	16.9568	<b>17.0564</b>
cameraman + noise	19.8663	20.2049	20.5898	<b>20.7447</b>
mandrill + noise	18.4550	18.4491	19.0649	<b>19.1834</b>

**Table 3:** The PSNR values for experiments involving downsampling and noise. Shearlet SME gives the best PSNR for all experiments, indicating the value of shearlets in the noisy regime.

Unlike in the downsampling plus blurring experiments, shearlet SME gives the best performance in 9/9 experiments. The strong performance, even in the presence of noise, can be attributed to the known effectiveness of shearlets for denoising [50]. Conversely, shearlets are not known to be superior to wavelets for deconvolution, which is the corresponding problem in the case of applying a Gaussian convolutional blur.

We note also that shearlet directional blurring performs more strongly in this regime, outperforming

linear cubic spline interpolation. This could be due to the fact that a blurring method will smooth out some of the noise, generating an improvement in  $\ell^2$  norm in some cases, and consequently improving PSNR as well.

### 5.5. Experiments with Downsampling, Noise, and Blurring

The final degradation operator considered is the combination of all the above degradation operators: downsampling by a factor of 2, followed by isotropic Gaussian blurring, followed by adding white noise. The blur is implemented by applying a low-pass Gaussian blur of size  $3 \times 3$  and standard deviation  $\sigma = .5$  to the already downsampled image. The Gaussian white noise is mean  $\mu = 0$ ,  $\sigma = .1$ .

Image	linear	shearlet blur	SME wavelet	SME shearlet
plane + noise + blur	22.6592	22.4552	23.2392	<b>23.4282</b>
circle + noise + blur	22.4743	22.5411	22.9182	<b>23.0321</b>
parabola + noise + blur	21.8357	21.7688	22.4522	<b>22.6575</b>
lidar + noise + blur	20.8218	21.2304	21.4115	<b>21.5070</b>
SAR + noise + blur	13.5794	13.5373	13.8079	<b>13.8536</b>
HSI + noise + blur	22.4182	22.9753	23.0389	<b>23.1278</b>
peppers + noise + blur	16.5811	16.0002	16.8466	<b>16.9114</b>
cameraman + noise + blur	19.8559	20.0352	20.4122	<b>20.5280</b>
mandrill + noise + blur	18.5582	18.5749	18.9838	<b>19.0640</b>

**Table 4:** The PSNR values for experiments involving downsampling, blurring, and noise. Shearlet SME outperforms all other methods in all experiments.

As was the case with downsampling alone, and downsampling combined with noise, SME with shearlets gives the best PSNR result for all experiments. This is particularly relevant, since this final regime is the most challenging degradation operator in the sense of (1).

### 5.6. Visual Analysis

In order to better understand our algorithm, we visually analyze one of our synthetic examples. The simple nature of this example gives a clearer insight into the methods, compared to analyzing a more complicated real image. A subset of the circle example appears in Figure 4.

In order to superresolve this region effectively, an algorithm must recover the jagged edges precisely, while also preserving the flat region at the top. The corresponding results of the algorithms considered in this paper appear in Figure 9. Shearlet SME gives the best resolution of the boundary: the jagged edge is well-approximated, and the flat top is also handled effectively. The jagged edge resolution is poorer for wavelet SME and cubic spline interpolation. The jaggedness is almost totally smoothed out

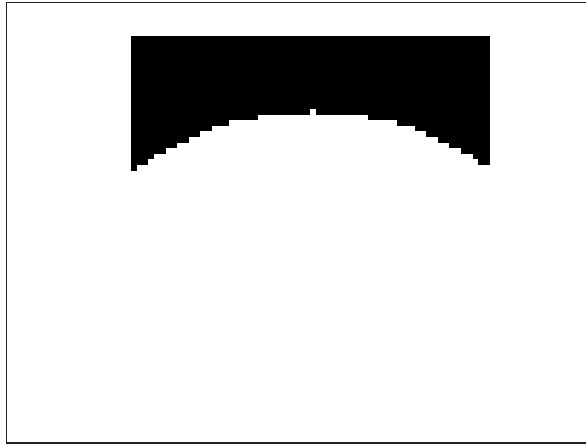


**Figure 4:** *A specific portion of the circle synthetic image, showing both flat and rapidly changing regions.*

by directional shearlet blurring, yielding a relatively poor PSNR results. Indeed, the shearlet SME image has a gradual transition along the boundary, while preserved the jagged edge. This is due to the efficiency of shearlets in resolving edges, as argued theoretically in Section 3.

## 6. Conclusions and Future Work

This article presented a superresolution algorithm based on sparse mixing estimators in a shearlet frame. Compared to the original wavelet-based algorithm of Mallat and Yu, our algorithm saw better overall performance in terms of PSNR, especially when the images were cartoon-like. Indeed, across 9 images with 4 types of degradation operators, only in 2 cases did SME with shearlets not give the best result. This record of 34/36 affirms the theory of shearlet systems, which are known to be theoretically near-optimal for cartoon-like images.

However, for images that are strongly textural, and thus very far from the cartoon-like regime, the performance of wavelets is potentially superior to that of shearlets. This is, from a mathematical standpoint, expected. Shearlets are not known to perform exceptionally well on signals without strong directional content. It is of interest to consider frames that are known to perform well for textures, such as wave atoms [68], for isotropic superresolution. Also of interest are approaches that incorporate directionality into windowed Fourier methods, such as directional Gabor systems [69]. These systems have both a Gabor structure, which is well-suited for textures, and a directional structure, which could potentially resolve edges well.

Studying how to decompose an image into different aspects that would be best handled by different frames is of great interest. Joint frames of wavelets and shearlets have been proposed to separate

textures from edges [70]. Such an approach could be useful for determining which features in an image should be treated directionally, and which isotropically. More generally, morphological component analysis (MCA) [36] is of interest, in order to superresolve different features in an image with different methods. MCA regularization terms have been included for superresolution [37], and it is of interest to incorporate frames with known optimality properties into this regime.

## 7. Acknowledgements

The authors thank David J. Harding of the NASA Goddard Space Flight Center for supplying the SAR image. In addition, the authors would like to thank the Hyperspectral Image Analysis group and the NSF Funded Center for Airborne Laser Mapping (NCALM) at the University of Houston for providing the lidar scene used in this study, and the IEEE GRSS Data Fusion Technical Committee for organizing the 2013 Data Fusion Contest.

## 8. References

### References

- [1] H. Greenspan. Super-resolution in medical imaging. *The Computer Journal*, 52(1):43–63, 2009.
- [2] M.D. Robinson, S.J. Chiu, J. Y. Lo, C. A. Toth, J. A. Izatt, and S. Farsiu. *New applications of super-resolution in medical imaging*. CRC Press, 2010.
- [3] J. Kennedy, O. Israel, A. Frenkel, R. Bar-Shalom, and H. Azhari. Super-resolution in pet imaging. *Medical Imaging, IEEE Transactions on*, 25(2):137–147, 2006.
- [4] A. Rueda, N. Malpica, and E. Romero. Single-image super-resolution of brain mr images using overcomplete dictionaries. *Medical image analysis*, 17(1):113–132, 2013.
- [5] A.J. Tatem, H.G. Lewis, P.M. Atkinson, and M.S. Nixon. Super-resolution target identification from remotely sensed images using a hopfield neural network. *Geoscience and Remote Sensing, IEEE Transactions on*, 39(4):781–796, 2001.
- [6] T. Kasetkasem, M.K. Arora, and P.K. Varshney. Super-resolution land cover mapping using a markov random field based approach. *Remote Sensing of Environment*, 96(3):302–314, 2005.



- [7] T. Akgun, Y. Altunbasak, and R.M. Mersereau. Super-resolution reconstruction of hyperspectral images. *IEEE Transactions on Image Processing*, 14(11):1860–1875, 2005.
- [8] Y. Zhao, J. Yang, Q. Zhang, L. Song, Y. Cheng, and Q. Pan. Hyperspectral imagery super-resolution by sparse representation and spectral regularization. *EURASIP Journal on Advances in Signal Processing*, 2011(1):1–10, 2011.
- [9] E.J. Candès and C. Fernandez-Granda. Towards a mathematical theory of super-resolution. *Communications on Pure and Applied Mathematics*, 67(6):906–956, 2014.
- [10] E.J. Candès and C. Fernandez-Granda. Super-resolution from noisy data. *Journal of Fourier Analysis and Applications*, 19(6):1229–1254, 2013.
- [11] W. Liao and A. Fannjiang. Music for single-snapshot spectral estimation: Stability and super-resolution. *Applied and Computational Harmonic Analysis*, 2014.
- [12] H. Demirel and G. Anbarjafari. Image resolution enhancement by using discrete and stationary wavelet decomposition. *Image Processing, IEEE Transactions on*, 20(5):1458–1460, 2011.
- [13] M.D. Robinson, C. Toth, J.Y. Lo, and S. Farsiu. Efficient fourier-wavelet super-resolution. *Image Processing, IEEE Transactions on*, 19(10):2669–2681, 2010.
- [14] L. Yue, H. Shen, Q. Yuan, and L. Zhang. A locally adaptive  $l_1$ – $l_2$  norm for multi-frame super-resolution of images with mixed noise and outliers. *Signal Processing*, 105:156–74, 2014.
- [15] J.J. Benedetto and W. Li. Super-resolution by means of Beurling minimal extrapolation. *arXiv:1601.05761*, 2016.
- [16] S. Mallat and G. Yu. Super-resolution with sparse mixing estimators. *IEEE Transactions on Image Processing*, 19(11):2889–2900, 2010.
- [17] K. Guo and D. Labate. Optimally sparse multidimensional representation using shearlets. *SIAM journal on mathematical analysis*, 39(1):298–318, 2007.
- [18] G. Kutyniok and W.-Q. Lim. Compactly supported shearlets are optimally sparse. *Journal of Approximation Theory*, 163(11):1564–1589, 2011.
- [19] W. Czaja, J.M. Murphy, and D. Weinberg. Superresolution of remotely sensed images with anisotropic features. In *Proceedings of SAMPTA*, 2015.

- [20] E. H. Bosch, A. Castrodad, J. S. Cooper, W. Czaja, and J. Dobrosotskaya. Multiscale and multidirectional tight frames for image analysis. In *Proceedings of SPIE, vol. 8750*, 2013.
- [21] S.C. Park, M.K. Park, and M.G. Kang. Super-resolution image reconstruction: a technical overview. *IEEE Signal Processing Magazine*, 20(3):21–36, 2003.
- [22] Moshe B.E., A. Zomet, and S.K. Nayar. Video super-resolution using controlled subpixel detector shifts. *IEEE Transactions on Pattern Analysis and Machine Intelligence*, 27(6):977–987, 2005.
- [23] V.P. Shah, N.H. Younan, and R.L. King. An efficient pan-sharpening method via a combined adaptive pca approach and contourlets. *IEEE Transactions on Geoscience and Remote Sensing*, 46(5):1323–1335, 2008.
- [24] W. Czaja, T. Doster, and J.M. Murphy. Wavelet packet mixing for image fusion and pan-sharpening. In *SPIE Defense+ Security*, 2014.
- [25] R. Keys. Cubic convolution interpolation for digital image processing. *IEEE Transactions on Acoustics, Speech and Signal Processing*, 29(6):1153–1160, 1981.
- [26] W.T. Freeman, T.R. Jones, and E.C. Pasztor. Example-based super-resolution. *Computer Graphics and Applications, IEEE*, 22(2):56–65, 2002.
- [27] S. Vishnukumar, M.S. Nair, and M. Wilscy. Edge preserving single image super-resolution with improved visual quality. *Signal Processing*, 105:283–97, 2014.
- [28] J. Yang, J. Wright, T.S. Huang, and Y. Ma. Image super-resolution via sparse representation. *IEEE Transactions on Image Processing*, 19(11):2861–2873, 2010.
- [29] S. Farsiu, M.D. Robinson, M. Elad, and P. Milanfar. Fast and robust multiframe super resolution. *IEEE Transactions on Image processing*, 13(10):1327–44, 2004.
- [30] W.T. Freeman, T.R. Jones, and E.C. Pasztor. Example-based super-resolution. *IEEE Computer Graphics and Applications*, 22(2):56–65, 2002.
- [31] Y.C. Eldar, P. Kuppinger, and H. Bölcskei. Block-sparse signals: Uncertainty relations and efficient recovery. *Signal Processing, IEEE Transactions on*, 58:3042–3054, 2010.
- [32] Y.C. Eldar and H. Bölcskei. Block-sparsity: Coherence and efficient recovery. In *Acoustics, Speech and Signal Processing, IEEE International Conference on*, 2009.

- [33] G.R. Easley, D. Labate, and W.-Q. Lim. Sparse directional image representations using the discrete shearlet transform. *Applied and Computational Harmonic Analysis*, 25(1):25–46, 2008.
- [34] D. Labate, W.Q. Lim, G. Kutyniok, and G. Weiss. Sparse multidimensional representation using shearlets. In *Proceedings of International Society for Optics and Phototronics: Optics and Phototronics*, 2005.
- [35] K. Guo, G. Kutyniok, and D. Labate. Sparse multidimensional representations using anisotropic dilation and shear operators. In G. Chen and M.J. Lai, editors, *Wavelets and Splines (Athens, GA, 2005)*, pages 189–201. Nashboro Press, 2006.
- [36] M. Elad, J.-L. Starck, P. Querre, and D. L. Donoho. Simultaneous cartoon and texture image inpainting using morphological component analysis (MCA). *Applied and Computational Harmonic Analysis*, 19(3):340–358, 2005.
- [37] W. Liu and S. Li. Sparse representation with morphologic regularizations for single image super-resolution. *Signal Processing*, 98:410–22, 2014.
- [38] I. Daubechies. *Ten lectures on wavelets*. Society for industrial and applied mathematics, 1992.
- [39] Stéphane Mallat. *A wavelet tour of signal processing*. Academic press, 1999.
- [40] M.V. Wickerhauser. *Adapted Wavelet Analysis from Theory to Software*. AK Peters Ltd., 1994.
- [41] R.A. DeVore, B. Jawerth, and B.J. Lucier. Image compression through wavelet transform coding. *IEEE Transactions on Information Theory*, 38(2):719–746, 1992.
- [42] K. Amolins, Y. Zhang, and P. Dare. Wavelet based image fusion techniques-an introduction, review and comparison. *ISPRS Journal of Photogrammetry and Remote Sensing*, 62:249–263, 2007.
- [43] I. Zavorin and J. Le Moigne. Use of multiresolution wavelet feature pyramids for automatic registration of multisensor imagery. *IEEE Transactions on Image Processing*, 14(6):770–782, 2005.
- [44] S. Dahlke, F. De Mari, P. Grohs, and D. Labate, editors. *Harmonic and Applied Analysis: From Groups to Signals*. Birkhäuser, 2015.

- [45] E.J. Candès and D.L. Donoho. New tight frames of curvelets and optimal representations of objects with piecewise  $C^2$  singularities. *Communications on pure and applied mathematics*, 57(2):219–266, 2004.
- [46] M.N. Do and M. Vetterli. Contourlets: a directional multiresolution image representation. In *Proceedings of 2002 IEEE International Conference on Image Processing*, 2002.
- [47] W. Czaja and E.J. King. Isotropic shearlet analogs for  $L^2(\mathbb{R}^k)$  and localization operators. *Numerical functional analysis and optimization*, 33(7-9):872–905, 2012.
- [48] W. Czaja and E.J. King. Anisotropic shearlet transforms for  $L^2(\mathbb{R}^k)$ . *Mathematische Nachrichten*, 287(8-9):903–916, 2014.
- [49] P.S. Negi and D. Labate. 3-D discrete shearlet transform and video processing. *IEEE Transactions on Image Processing*, 21(6):2944–2954, 2012.
- [50] G.R. Easley, D. Labate, and F. Colonna. Shearlet-based total variation diffusion for denoising. *IEEE Transactions on Image Processing*, 18(2):260–268, 2009.
- [51] J.M. Murphy and J. Le Moigne. Shearlet features for registration of remotely sensed multitemporal image. In *Proceedings of IGARSS*, 2015.
- [52] E.J. King, G. Kutyniok, and X. Zhuang. Analysis of inpainting via clustered sparsity and microlocal analysis. *Journal of mathematical imaging and vision*, 48(2):205–234, 2014.
- [53] Q. Miao, C. Shi, P.-F. Xu, M. Yang, and Y.-B. Shi. A novel algorithm of image fusion using shearlets. *Optics Communications*, 284(6):1540–1547, 2011.
- [54] G. Kutyniok and D. Labate. *Shearlets: Multiscale analysis for multivariate data*. Springer Science & Business Media, 2012.
- [55] G. Kutyniok, M. Shahram, and X. Zhuang. Shearlab: A rational design of a digital parabolic scaling algorithm. *SIAM Journal on Imaging Sciences*, 5(4):1291–1332, 2012.
- [56] S. Häuser. Fast finite shearlet transform. *arXiv preprint*, arXiv:1202.1773, 2012.
- [57] X. Gibert, V.M. Patel, D. Labate, and R. Chellappa. Discrete shearlet transform on gpu with applications in anomaly detection and denoising. *EURASIP Journal on Advances in Signal Processing*, 2014(1):1–14, 2014.

- [58] J.J. Benedetto. *Harmonic analysis and applications*. CRC Press, 1996.
- [59] S. Häuser and G. Steidl. Fast finite shearlet transform: a tutorial. *Arxiv*, 1202.1773, 2014.
- [60] G. Kutyniok and D. Labate. Resolution of the wavefront set using continuous shearlets. *Transactions of the American Mathematical Society*, 361(5):2719–2754, 2009.
- [61] D.E. Weinberg. *Multiscale and Directional Representations of High-Dimensional Information Content in Remotely Sensed Data*. PhD thesis, University of Maryland, College Park, 2015.
- [62] Hyperspectral remote sensing scenes. [http://www.ehu.eus/ccwintco/index.php?title=Hyperspectral\\_Remote\\_Sensing\\_Scenes](http://www.ehu.eus/ccwintco/index.php?title=Hyperspectral_Remote_Sensing_Scenes). Accessed 12-01-2015.
- [63] 2013 IEEE GRSS Data Fusion Contest. <http://www.grss-ieee.org/community/technical-committees/data-fusion-contest/>. Accessed 8-14-2015.
- [64] Public-domain test images for homeworks and projects. <https://homepages.cae.wisc.edu/~ece533/images/>. Accessed 12-01-2015.
- [65] SIPI Image Database. <http://sipi.usc.edu/database/>. Accessed 12-01-2015.
- [66] E.H. Bosch, W. Czaja, J.M. Murphy, and D. Weinberg. Anisotropic representations for superresolution of hyperspectral data. In *SPIE Defense+ Security. International Society for Optics and Photonics*, 2015.
- [67] J.M. Murphy. *Anisotropic Harmonic Analysis and Integration of Remotely Sensed Data*. PhD thesis, University of Maryland, College Park, 2015.
- [68] L. Demanet and L. Ying. Wave atoms and sparsity of oscillatory patterns. *Applied and Computational Harmonic Analysis*, 23(3):368–387, 2007.
- [69] L. Grafakos and C. Sansing. Gabor frames and directional time-frequency analysis. *Applied and Computational Harmonic Analysis*, 25(1):47–67, 2008.
- [70] D. Donoho and G. Kutyniok. Geometric separation using a wavelet-shearlet dictionary. In *SAMPTA*, 2009.



**Figure 5:** *Linear cubic spline interpolation.*

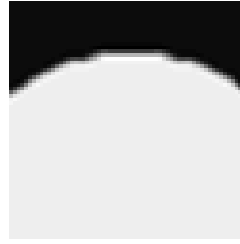


**Figure 6:** *Directional shearlet blurring.*



**Figure 7:** *Wavelet SME.*



**Figure 8:** *Shearlet SME.*

**Figure 9:** *Results of applying the superresolution algorithms to the image in Figure 4.*